Journal of Materials Chemistry A

On the dynamics of transition metal migration and its impact on the performance in layered oxides for sodium-ion batteries: $NaFeO_2$ as a case study.

Journal:	*Journal of Materials Chemistry A*
Manuscript ID	TA-ART-03-2018-002473.R2
Article Type:	Paper
Date Submitted by the Author:	03-Jul-2018
Complete List of Authors:	Silván, Begoña; CIC energiGUNE, Gonzalo, Elena; CIC Energigune, Power Storage, Batteries Djuandhi, Lisa; University of New South Wales School of Chemistry Sharma, Neeraj; UNSW Australia, Chemistry; Fauth, Francois; ALBA Light Source, Saurel, Damien; CIC energiGUNE,

Journal Name

ARTICLE

On the dynamics of transition metal migration and its impact on the performance in layered oxides for sodium-ion batteries: $NaFeO_2$ as a case study.

Received 00th January 20xx,
Accepted 00th January 20xx

DOI: 10.1039/x0xx00000x

www.rsc.org/

Begoña Silván,[a] Elena Gonzalo,*[a] Lisa Djuandhi,[b] Neeraj Sharma,[b] François Fauth[c] and Damien Saurel*[a]

Transition metal (TM) layered oxides constitute one of the most promising family of compounds for the cathode of Na-ion batteries. However, their structural stability at charged state is a critical performance limiting factor, which is believed to be closely related with irreversible TM migration into the Na layers. Nevertheless, experimental evidence of this TM migration and its influence on the electrochemical performance is still scarce, while the understanding of such a phenomenon constitutes a key step for developing better performing TM layered oxides. Here $NaFeO_2$ has been studied as a model system, since it is expected to produce one of the most pronounced TM migration and provide possibly one of the highest theoretical energy density of TM layered oxides. By combining Potential Intermittent Titration Technique (PITT), Electrochemical Impedance Spectroscopy (EIS) and *operando* X-ray diffraction it has been possible to analyze the structural evolution of Na_xFeO_2, track the iron migration and observe their influence on the insertion capacity and Na diffusivity.

Introduction

The development of the use of alternative (renewable) energy sources and electric vehicles (EVs) is one of the main challenges to reduce the dependency on fossil fuels. Renewable energy sources generally produce variable output as a function of time, and therefore similar to EVs they require energy storage technologies. This has induced tremendous pressure on the development of suitable secondary battery technologies that are safe, low cost and deliver excellent performance. Nowadays lithium-ion batteries (LIBs) are leading the secondary battery market, but recent concerns on potential lithium scarcity and consequently the increase of raw material price has motivated a strong research effort on alternative secondary battery technologies.[1] Thanks to its strong similarities to the established LIB technology, sodium-ion battery's (SIB) research is growing as a potential lower cost drop-in alternative technology.[2–4] Na is abundant and evenly spread on the Earth's crust, and works with cheaper and lighter aluminium current collectors at the anode, allowing replacement of the more expensive and heavier copper current collector used in LIBs.[5] However, sodium is bigger and heavier than lithium, affecting mass diffusion and specific capacity.[3–6] This coupled with the usually lower voltages compared to LIBs,[7] lead to lower energy densities which needs to be improved to become competitive in the battery market.[8,9] Sodium based layered oxides have been widely studied because they are relatively easy to synthesize, are versatile and show some of the best specific energies. Although these materials have not reached the performance of the best lithium-based equivalents, the fact that a larger number of stable phases have been reported for sodium provides hope for finding a competitive material on both the performance and cost point of view. Research is thus targeted to improve the electrochemical performance of sodium based TM layered oxides whilst maintaining low prices, especially on compositions rich in cheap and abundant TMs such as iron or manganese.[10,11] However, two serious issues to be tackled, and to-date only superficially explored, are the stability of the layered structure at high state of charge, and the sodium deficiency at the pristine state that most of the best performing compounds present, e.g. $Na_{2/3}TMO_2$ compositions. The sodium deficient pristine phases, which usually present a P2 structure as named by Delmas *et al.*,[12] tend to show better stability at high state of charge, but their sodium deficiency limits the first cycle Coulombic efficiency and hence the available specific energy at full cell level. This has driven the development of pre-doping strategies.[13,14] In the case of $NaFeO_2$ and $NaCrO_2$ the lack of stability of the structure at high state of charge has been demonstrated to be related with TM migration to the Na layer, which tends to shrink the interlayer distance, hence limiting the available capacity and the

[a] CIC Energigune, Parque Tecnológico de Álava. Albert Einstein 48, Ed. CIC, 01510 Miñano, Spain. *Emails: egonzalo@cicenergigune.com, dsaurel@cicenergigune.com
[b] School of Chemistry, UNSW Australia, Sydney, NSW 2052, Australia.
[c] Experiments Division, CELLS - ALBA, Carrer de la Llum 2-26, 08290 Cerdanyola del Vallès, Barcelona, Spain.
Electronic Supplementary Information (ESI) available: See DOI: 10.1039/x0xx00000x

cycle stability by blocking Na diffusion.[15,16] Irreversible TM migration into the alkali metal slabs appears to be a common issue in many layered oxides, for SIBs as well as LIBs.[15,17–20] It has been assigned to the low activation barrier for TM ions to migrate and electrostatic repulsion between neighbouring atoms in the TM layer.[17,18] This effect has been found to be mitigated by substitutions on the TM site leading to ternary or quaternary compounds.[15] However, this may induce a significant increase of the cost by reducing the amount of abundant metals such as Fe or Mn, substituting them by more expensive TM such as Ni, Mg, Ti or Co.[21–25] Such substitutions have to be ideally avoided as elemental supply has been identified as a critical bottleneck issue for the development of LIBs.[26] There is thus an urgent need to find a suitable strategy for developing TM layered oxide compounds that allows the practical use of most of their theoretical capacity, with no sodium deficiency and based on abundant TMs.

Within this scope, the present work aims at tackling the issue of the structural instability at high state of charge related to the TM migration to the Na layers. For this purpose, α-$NaFeO_2$ has been chosen as a model system as it is known to present the strongest effect of TM migration, affecting its performance if charged beyond about 40% of its theoretical capacity.[15,19,20] A few recently reported works have shed some light on $NaFeO_2$'s limitations and structure-electrochemical relationships. Lee *et al.* reported a very peculiar charge-discharge mechanism with a pinning of the initial O3 phase ascribed to Fe migration to the sodium layers,[19] which differs from the structural evolution reported for other O3 TM oxides.[15] Additionally, based on DFT calculations Li *et al*. demonstrated that the energy barrier for Fe migration reduces as the Fe content increases in Fe rich TM oxides.[15] They also highlighted, based on a HRTEM (high-resolution transmission electron microscopy) study of cycled materials, that TM migration is present in large amount in $NaFeO_2$ when discharged from 4.5 V, while it is not detectable in the case of quaternary Fe-containing layered compounds. However, the role of the sodium content, and especially the composition at which iron migration starts to occur, remains to be ascertained. Moreover, a clear correlation between sodium ionic diffusion and TM migration remains to be experimentally demonstrated. Finally, it is still unclear why the mechanism of phase transformation in $NaFeO_2$ is different from other O3 TM oxides.

In the present paper a detailed study of the reaction mechanism, including the evolution of Fe migration, and the reaction kinetics of O3-$NaFeO_2$ layered oxide is presented. The combination of PITT, EIS and *operando* PXRD measurements shed a new light on the mechanism of charge storage in O3- Fe-rich layered oxides, the TM metal migration and its influence on the kinetics of charge storage.

Experimental

Material synthesis and characterization.

O3-$NaFeO_2$ was synthetized by solid state reaction. Anhydrous sodium carbonate (Na_2CO_3) and iron (II,III) oxide (Fe_3O_4) were mixed and grinded. The pelletized material was thermally treated at 650°C during 15h in air and slowly cooled to room temperature.

Structural characterization was investigated by X-ray diffraction (XRD, Bruker D8 Discover) using monochromatic Cu-Kα_1 wavelength with a LYNXEYE detector and with sufficient discrimination to avoid fluorescence from iron. The sample was mounted in an airtight sample holder and measured in the 2θ range of 15°-80°. Rietveld refinement was undertaken with the FullProf software suite.[27] The sample was characterized with scanning electron microscopy (SEM, FEI Quanta 200FEG microscope) to determine particle morphology and size.

Electrochemical performance testing.

The material was electrochemically tested in Swagelok-type cells, using metallic Na as counter electrode. Composite electrodes were prepared by mixing active material, Super C65 carbon and PVdF (polyvinylidene fluoride) binder in 80:10:10 wt.%, proportion respectively, and dissolved in NMP (N-Methyl-2-pyrrolidone). The slurry was cast on aluminium foil with an approximate active material loading of 2 mg cm^{-2} and vacuum dried at 80°C overnight. Whatman GF D55 glass fibre separator was soaked in 1M $NaClO_4$ EC:PC (1:1 w/w) (ethylene carbonate: propylene carbonate) electrolyte. All processes were carried out inside an argon filled glove box to avoid atmospheric moisture contamination. The cells were tested with a VMP3 Bio-logic potentiostat at C/10 current rate (24.18 mA g^{-1}).

***In-situ* XRD.**

In-situ XRD measurements were performed using a Bruker D8 Advance diffractometer in reflexion mode, with non-monochromatic Cu-Kα or Co-Kα sources and LYNXEYE detector. These experiments used the previously reported electrochemical cell developed at CIC Energigune.[28,29] This custom designed cell uses an X-ray transparent aluminium covered beryllium window as positive current collector. $NaFeO_2$ powder was mixed with Ketjenblack carbon in an 80:20 wt.% proportion to be used as working electrode, and metallic Na was used as counter electrode. Two Whatman GF D55 glass fibre separators were soaked in 1M $NaClO_4$ EC:PC (1:1 w/w) electrolyte and placed between the electrodes. The cells (*cell 1*, *cell 2* and *cell 3*) were galvanostatically charged at a slow rate (C/30, 8.06 mA g^{-1}) using a VMP3 Bio-logic potentiostat. XRD scans were collected *operando* every 30 minutes in the 2θ range of 15°-45° (*cell 1*), 18°-21° and 40°-51° (*cell 2*) and 17°-51° (*cell 3*). In addition, in the case of *cell 3*, a XRD measurement of 66h has been performed after 48h relaxation in open circuit voltage (OCV) after charging to 4V. The same *cell 3*, after further discharge to 1.5V followed by 12h relaxation, were measured at the Materials Science and Powder Diffraction (MSPD) beamline[30,31] at the ALBA Synchrotron for a snapshot in transmission mode (beamsize 1.5 x 5 mm^2 to 0.015 x 0.015 mm^2). To allow the beam transmission through the cell, the current collector on the sodium side has a 2 mm diameter hole and the plunger uses a transparent beryllium window. In these

experiments 30 second patterns were recorded on a Mythen detector using a wavelength (λ) of 0.8255 Å.

Operando HRXRD measurements were carried out at the Powder Diffraction beamline[32–34] of the Australian Synchrotron using a modified coin cell, with Kapton covered 3 mm diameter holes in the casing and 5 mm diameter hole in stainless steel spacer. The coin cell contained Na metal, glass fibre separator soaked in $NaClO_4$ EC:PC (1:1 w/w) and a laminate electrode casted on aluminium foil. Further details can be found in previous work.[35,36] The wavelength was λ = 0.6882 Å, and the beamsize was 5 x 2 mm^2. During galvanostatic cycling a pattern was recorded every 30 minutes with 3.4 minutes of acquisition time.

PITT.

Potentiostatic Intermittent Titration Technique (PITT) was used to determine ionic diffusion coefficient. The PITT was performed upon charge and discharge by successive constant potential steps of 25 mV during which the current was allowed to relax down to 0.5 mA g^{-1}, corresponding to C/500. The diffusion coefficient was estimated from PITT measurements according to:

$$D = \frac{1}{2}\left[\frac{1}{A_W}\frac{V_m}{FS}\frac{\partial E}{\partial x}\right]^2 \qquad (1)$$

where V_m is the molar volume of the intercalation compound, F is Faraday's constant, A_W the Warburg coefficient of the semi-infinite bulk diffusion and S is the electrochemically active specific surface area of the material.[37–39]

A_W was deduced from the current relaxation as:[37,38]

$$A_W = \frac{1}{\sqrt{2\pi t}}\frac{\Delta E}{I} \qquad (2)$$

where $\boldsymbol{\Delta E}$ is the potential step, I the cottrelian current and t the time from the beginning of the step. Specific surface area S was estimated from SEM measurements. Due to the layered nature of the sample, inducing two-dimensional ionic conductivity, the electrochemically active specific surface was considered to be 2/3 of the measured specific surface area.

In-situ EIS.

Using a VMP3 Biologic potentiostat the cell was charged with 25 mV steps and the current was allowed to relax for 4 hours before EIS measurements to ensure that an equilibrium state was reached. A sinusoidal voltage (with an amplitude of 10 mV and frequency ranging from 200 kHz to 2 mHz) was applied around the equilibrium DC voltage value, and output current and phase changes were measured. The obtained impedance data (Z = V/I) were analysed by fitting to an equivalent circuit combining resistors and constant phase elements.

When the semi-infinite linear diffusion conditions were achieved, the diffusion coefficient was determined from the mass diffusion part of the EIS spectra using equation (1) and calculating the Warburg impedance as:

$$A_W = -\mathrm{Im}[\mathrm{Z}]/\sqrt{\mathrm{f}} \qquad (3)$$

where f stands for frequency.

Results and discussion

The XRD pattern and Rietveld analysis of the pristine sample are represented in Fig. 1a. It is indexed in the $R\bar{3}m$ space group, with an O3 layered oxide structure as named by Delmas *et al*.,[12] where Na ions occupy octahedral sites between Fe-O layers and oxide layers are stacked as …ABC ABC… The cell parameters obtained from the refinement are $a = b = 3.02262(6)$ Å, $c = 16.0916(5)$ Å, α = β = 90° and γ = 120°, and are in good agreement with previously reported results.[19,20] All the structural parameters can be found in supplementary information, Table S1. No extra peaks ascribed to impurities are observed. SEM images are presented in Fig. 1b and 1c, with x1500 and x60000 magnifications, respectively. They show spherical shaped submicron sized primary particles with an average size of 250 nm in diameter, forming aggregates of different sizes (from 5 µm up to 200 µm). Voltage vs. capacity curves are presented in Fig. 2a for the 1st, 5th, 10th and 50th cycles of a cell cycled in the voltage range V = 2.5-3.5 V. These curves present the typical behaviour known for this material, i.e. a flat voltage-capacity profile around 3.3 V corresponding to $Fe^{III/IV}$ oxidation,[40,41] with an initial reversible capacity of 112 mA h g^{-1} at C/10 (97 mA h g^{-1} at 1C, Fig. 2b) and nearly 80 mA h g^{-1} at the 50th cycle at C/10, which corresponds to 71% capacity retention. The Coulombic efficiency has an initial value of 86%

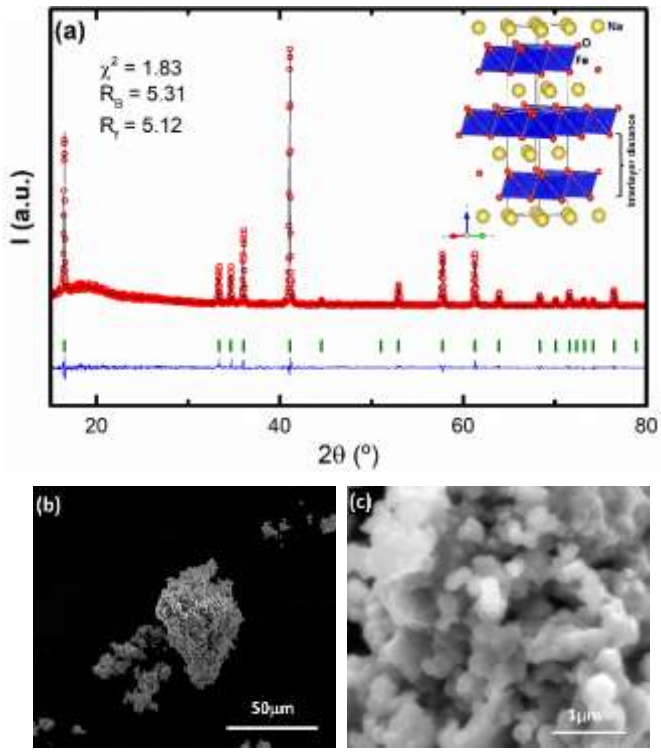

Fig. 1. (a) Rietveld-refined fit of the $NaFeO_2$ structrual model using $R\bar{3}m$ space group to the XRD data. In the inset, schema of the O3 layered structure. In this paper, interlayer distance will be considered as $c/3$, as shown in the image. (b) and (c) SEM images of powder material with x1 500 and x60 000 magnification respectively.

at C/10 (91% at 1C, Fig. S1b), reaches 96% at the second cycle at C/10 and remains constant at around 98% from the 10th cycle (see Fig. S1a). The obtained results show improved capacity and capacity retention compared to those previously reported for this material.[19,20] This is most likely related to the smaller particle size obtained in this work compared to literature (see Table S2 in supporting info). It is well known that smaller particle size tend to improve electrochemical performance by increasing the electrochemically active surface area and reducing diffusion path of alkali ions.[42] Note that an overpotential peak is observed at the beginning of the 3.3 V plateau during the first charge, marked with a red circle in Fig. 2a, which only appears at the first cycle. Figure 2b presents the reversible capacity evolution for this cell during the first 50 cycles (blue square markers), compared to a similar cell for which the upper limit of the voltage window has been gradually increased (red squares). Charging this material beyond 3.7 V leads to a fast capacity fading, in accordance with previous studies.[20,43] Fig. S2 displays the first cycle of three cells that have been charged to different maximum voltages at C/10 (24.18 mA g^{-1}). It appears clearly from this figure that as the maximum charge voltage is increased, the polarization of the cell is increased inducing a decrease of the reversible capacity, as previously reported by Yabuuchi et al..[20]

The results of the EIS measurements at various states of charge are presented in Fig. 3. The equilibrium voltage curve vs. capacity (blue solid line) is presented in Fig. 3a, the Nyquist plots of the EIS are presented in Figs. 3c-h at various state of charge, while the resistance values deduced from the fit of the EIS data are presented in Fig. 3b. As can be observed from Fig. 3a, the evolution of the equilibrium voltage vs. the charge capacity presents a very similar profile to the galvanostatically charged cells, shown in Fig. 2a.

The equivalent circuit used for fitting, shown in the inset of Fig. S3, contains resistors (*R*), constant phase elements (*C*) and Warburg elements (*W*).[44] Constant phase elements have been used instead of capacitors to take into account the influence of particle size distribution, electrode tortuosity and surface roughness. R_1 at high frequencies corresponds to the electrolyte's and cell's contact resistances. The second block ($R_2||C_2$) at medium frequencies has been assigned to surface contributions. In the low frequency zone, the third block (R_3+$W_3||C_3$) corresponds to charge transfer (R_3), electrical double layer capacitance -EDLC- (C_3) and mass diffusion (W_3 Warburg element). As can be seen in Figs. 3c-h, there is a very good agreement between the model (continuous lines) and the experimental measurements (symbols) at all states of charge.

As shown Fig. 3b, while R_1 and R_2 present limited changes during the whole charge, R_3 value varies by several orders of magnitude. The evolution of this resistance value presents a peak that corresponds to an increase of 3 orders of magnitude at the beginning of charge, immediately followed by a decrease of 4 orders of magnitude as the voltage arrives to the first plateau. It appears to be correlated with the overpotential that is observed at the beginning of the first charge during galvanostatic cycling (see the area marked with a red circle in Fig. 2a). Interestingly, the voltage peak is not observed in the

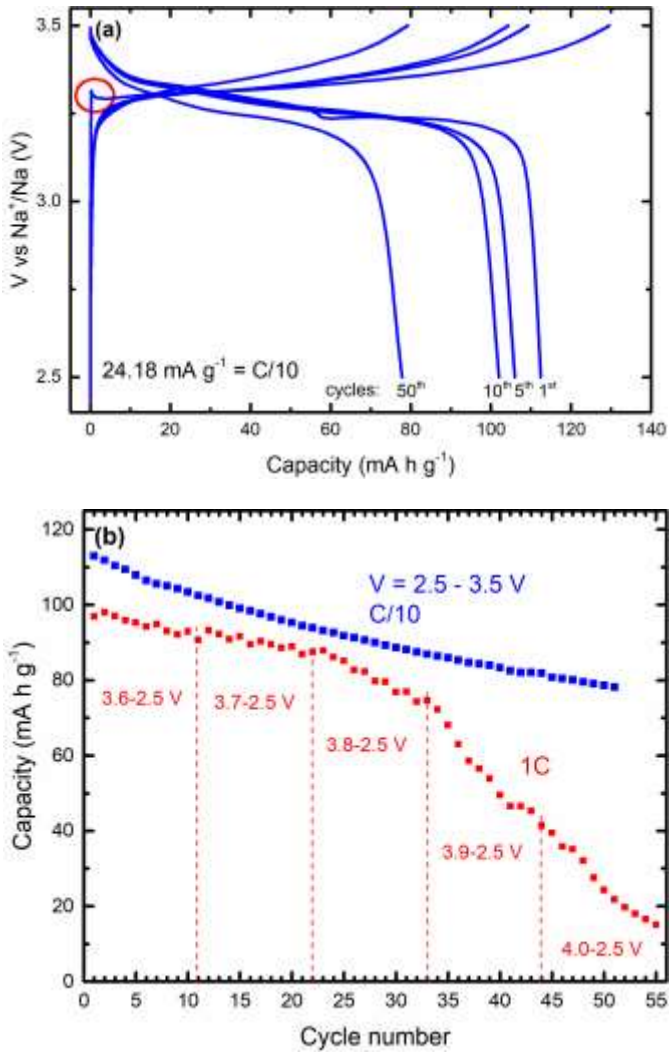

Fig. 2. (a) Voltage vs. capacity curves in the voltage at C/10 range of V = 3.5-2.5 V for cycles 1st, 5th, 10th and 50th. Marked with the red circle, overpotential previous to the first plateau during first charge. (b) Discharge capacity vs. cycle number at C/10 (24.18 mA g^{-1}) in the voltage range V = 3.5-2.5 V (solid blue squares) and at 1C (241.84 mA g^{-1}) with different upper voltage limits (red squares).

equilibrium voltage-capacity profile of Fig. 3a. This indicates that the overpotential that appears in constant current mode does not correspond to the thermodynamic equilibrium. It is thus a dynamic effect induced by a strong increase of the impedance of the cell, as reflected by the peak in R_3 resistance. After this peak, the R_3 resistance value remains constant during the plateau at 3.3 V. It then shows a progressive increase and by the end of the charge it has increased by more than two orders of magnitude. The charge transfer resistance increase at the end of charge can be due to a drop in electronic or ionic conductivity within the charge transfer region. As the charge transfer resistance is expected to be affected by poor electronic or ionic conductivity,[45] this increase of R_3 appears in accordance with previous studies suggesting a decrease of the ionic conductivity due to the migration of iron into the sodium slabs.[15,19] Within this scope, the overpotential peak observed at beginning of charge can be interpreted as a concentration

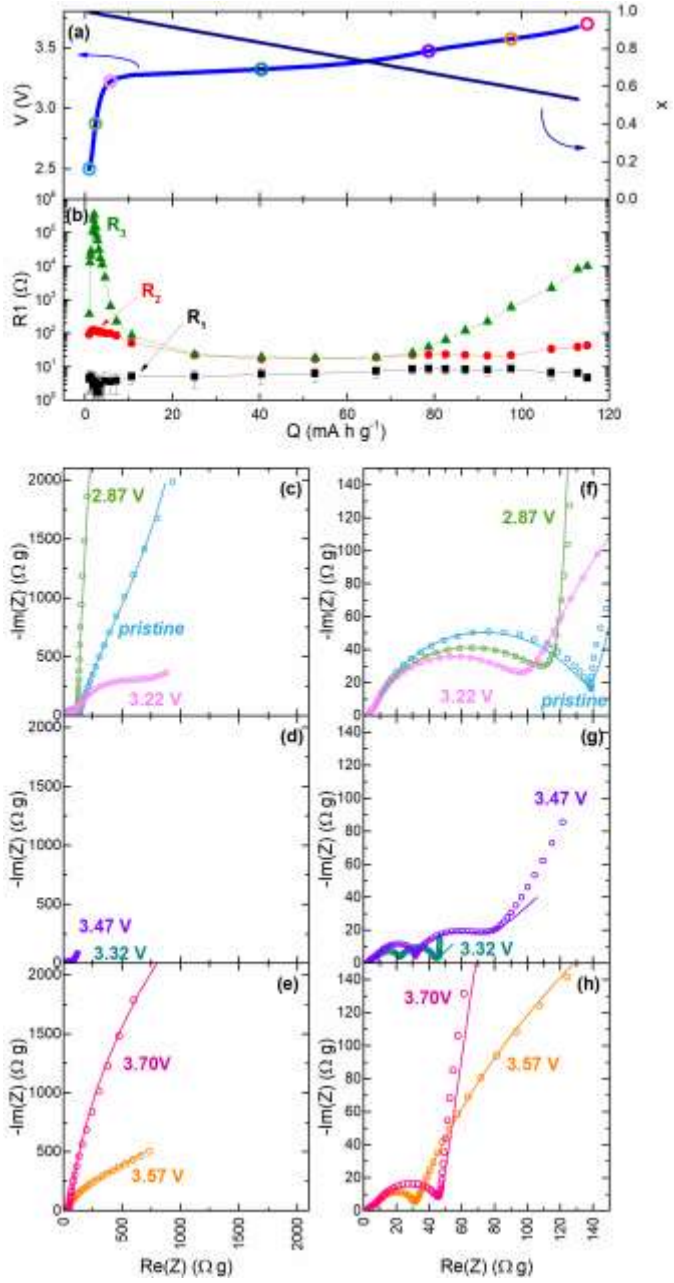

Fig. 3. (a) Equilibrium voltage (solid blue line) and derivative of the capacity (black dashed line) curves vs. capacity of the cell charged with potentiostatic steps. (b) R values of the refined Nyquist plots. Experimental (scatter) and fitted (lines) Nyquist plots at various charge states: (c,f) pristine state and beginning of charge at 2.87 V; (d,g) at half charge where charge transfer resistance is reduced at 3.22 V, 3.32 V and 3.47 V; and (e,h) beyond 3.5 V where charge transfer resistance is increased again at 3.57 V and 3.70 V. In Fig. 3a the voltage value at which these measurements were taken are indicated with circles.

overpotential suggesting a depletion at the surface of the active material when the redox reaction takes place.

As seen in Figs. 3c, d, and e, a ≈ 45° slope, typical response of semi-infinite linear mass diffusion (Warburg), is only observed during the voltage plateau (Fig. 3d), while at the beginning of charge (Fig. 3c) as well as beyond 3.5 V (Fig. 3e) the values of R_3 are so large that the corresponding medium frequency semicircle (second semicircle, Figs. 3f, g, h) overwhelms the Warburg impedance, impeding the estimation of its value. It is thus not possible, from our EIS measurements, to determine the evolution of the Warburg impedance, and hence of the mass diffusion, at beginning of charge as well as beyond 3.5 V.

In order to get a better understanding of the possible changes in the diffusion during charge and discharge, PITT measurements were performed during several cycles, progressively increasing the voltage windows (see Fig. 4a). The first two cycles were performed within the conservative voltage window (2.5 V to 3.4 V), and it was afterwards increased to 1.25-3.8 V, and finally to 1.25-4.0 V.

The PITT voltage curve is presented in Fig. 4a as a function of sodium content after relaxation to 0.5 mA g^{-1}. During the first cycles, below the reversible voltage limit, the curve is very similar to the galvanostatic cycling presented in Fig. 2a, with a good reversibility (black and grey lines in Fig. 4a). When the cell is charged beyond 3.5 V there is a strong increase of the voltage hysteresis from less than 50 mV when charged to 3.4 V, to about 1.5 V when charged to 3.8 V or higher. This is due to a strong decrease of the discharge potential, while the average charge potential remains marginally affected. Surprisingly, by opening the lower limit of the voltage window from 2.5 V down to 1.25 V, a non-negligible discharge capacity is achieved and maintained from one cycle to the other; $\Delta x \approx 0.3$ is reversibly extracted, which is 70% of the initial charge capacity obtained in the conservative window (2.5-3.4 V). This demonstrates that if the voltage window is enlarged the reaction is actually partially reversible.

Fig. S4 presents the potential and current evolution over time of a cell that has been discharged from 4 V down to 1.5 V, followed by a hold of 10 hours at 1.5 V and a relaxation in open circuit of more than 10 h. It appears clearly that after 10 h of hold at 1.5 V the current is still non-negligible, indicating that the reaction would need more time to be completed which suggests kinetic limitation. Also, during the 10h OCV period, the potential is neatly increasing from 1.5 V up to 2.1 V, and at the end is still evolving with a non-negligible slope. This infers that the lower discharge potential observed in PITT when discharged from 4 V does not correspond to a decrease of the thermodynamic equilibrium reaction potential but is rather related to a kinetically induced polarization of the cell which would need a much higher relaxation time to disappear. This over-polarization during discharge when the material is charged above 3.6 V is probably the main source of capacity fading when cycled in a narrow voltage window.

The effective diffusion coefficient D has been estimated from the current relaxation using equation 1 when semi-infinite diffusion conditions are fulfilled, i.e. when the current decays as $1/\sqrt{t}$, t being the time elapsed since the beginning of the PITT voltage step. Fig. 4b presents the values of D obtained at the beginning of the charge (BOC) for all charges, and at the beginning of discharge (BOD) when previously charged at 3.8 V or 4 V, along with the voltage window of the previous charge (Fig. 4c). The evolution of voltage, current and sodium content during the whole cycling can be found in supplementary information (Fig. S5), as well as values of D at all states of charge and discharge deduced from the PITT measurement and from the EIS data of Fig. 3 (Fig. S6). Note that the data are presented on a linear scale in Fig. 4b, while it is usually presented on a

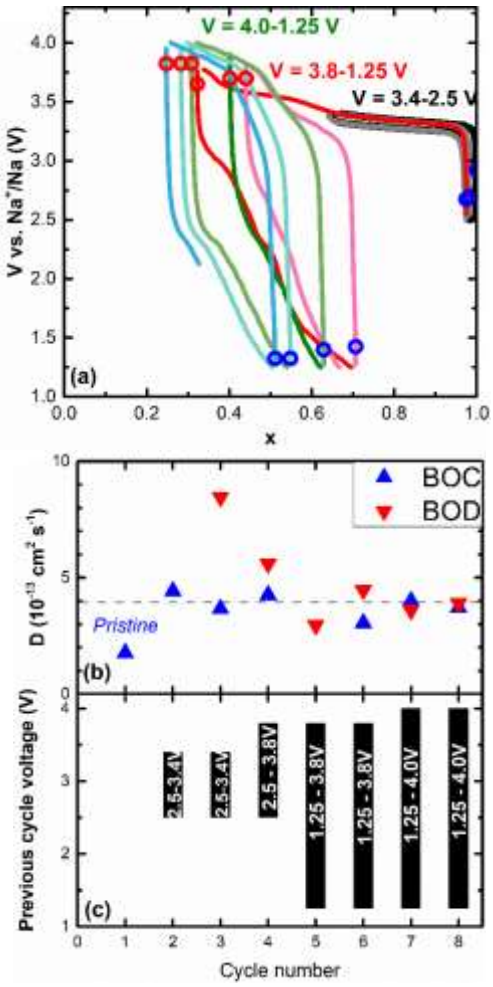

Fig. 4. (a) Equilibrium voltage vs. Na content curves of PITT cycling at different voltage windows. (b) Diffusion coefficients obtained at beginning of charge (BOC, blue up triangles) and discharge (BOD, red down triangles). Dashed line is visual help. Note that data are presented in linear scale. In Fig. 4a it is shown with blue and red circles the points where diffusion coefficients were calculated. (c) Voltage windows at which the cell was cycled before measuring each coefficient from panel (b).

logarithmic scale as changes of several order of magnitude are common for such measurements. Although the cell has been cycled in both the conservative (below 3.5 V) and non-conservative (beyond 3.5 V) voltage windows, the diffusion coefficient values remain essentially the same at BOC and BOD, and close to its value before cycling, around 4×10^{-13} cm^2 s^{-1}, despite the strong increase of the equilibrium cell polarization mentioned above. Furthermore, the effective diffusion coefficient stays constant over 8 cycles, the last 4 cycles being in the non-conservative voltage window. Thus it appears reasonable to conclude that the decrease of the average discharge potential when discharged from 3.8 V or 4 V is not related to a change of the effective diffusion coefficient.

This is a very surprising result, since it was previously proposed that the migration of Fe in the sodium layers observed at the end of charge strongly affects the sodium diffusion, which should be reflected in the D values at the beginning of the discharge as well. A strong decrease of D is actually observed during charge, as seen in Fig. S6, with a minimum centred at 3.3 V, which corresponds to the voltage plateau in Fig. 4a, followed by an increase of D at larger voltages. As can be seen in Fig. 4a, when the material is charged to 3.4 V the reaction is reversible with very small polarization between charge and discharge, suggesting that Fe migration has not occurred yet and that there is no source of over-polarization. The occurrence of such minimum of D during redox reaction is a typical feature of bi-phasic reactions, such as in the case of graphite or $LiFePO_4$ in Li-ion batteries.[37,46] It is an artefact due to application of single phase ionic diffusion theory into a two phase regime. As seen in Fig. S6, D increases above 3.3 V, reaching a maximum at around 3.45 V ($x \approx 0.6$), after which it decreases again. This second decrease of D corresponds to the increase of charge transfer resistance observed in the EIS experiment of Fig. 3a, which was ascribed to the migration of Fe. This confirms that the migration of Fe upon charge beyond 3.45 V actually affects the sodium diffusion, in addition to the strong increase of charge transfer resistance observed in Fig. 3. However, at the beginning of discharge, despite of the very high polarization remaining even after PITT relaxation (see Fig. 4a), as seen in Fig. S6 the D value deduced from the PITT current relaxation has recovered the value observed at the beginning of charge. This suggests that the inversion of the current, and, as a consequence, the large polarization that appears, reverses the effect of Fe migration on the diffusion.

This asymmetry observed between charge, where D_{EIS} drops while the reaction voltage is marginally affected, and discharge where D_{PITT} is recovered but a large polarization is observed, is probably related with the reaction topology. Indeed, upon charge sodium is extracted from $NaFeO_2$, which appears to be a rather good conductor looking at the low polarization observed when cycled below 3.5 V. In this case, supposing the reaction is inhomogeneous, the nucleation of Na poor regions with migrated Fe would not significantly affect the polarization. EIS measurements, however, would sense a change in D as it is based on an oscillation of the state of charge, i.e. successive slight charge and discharge incursions due to the sinusoidal voltage stimulus. When the discharge occurs, sodium needs to be reinserted into Na-poor Na_xFeO_2 which would be prevented by the presence of iron migrated into the sodium site, inducing an increase of the polarization. Two cases can be considered. i) Iron stays in the sodium layers, the over-polarization upon discharge is due to more difficult sodium diffusion in the charged state. According to the present PITT measurements it is clearly not the case as the effective diffusion coefficient at BOD and BOC is the same as that found in the pristine phase, and is not affected by the voltage at which the cell has been previously charged. ii) The over-polarization during discharge corresponds to the electromotive force or energy barrier overcoming needed to induce the return of iron from the sodium layers to the metal-oxide layers. This discharge-related over-polarization would as well be responsible for the increase of charge transfer resistance in the EIS experiment upon charge, due to the oscillating nature of this technique. The fact that this is not reflected in the value of the effective diffusion coefficient deduced from PITT measurements at BOD indicates that this over-polarization is constant at the scale of a PITT step, and has thus no signature on the current relaxation. In other words, this

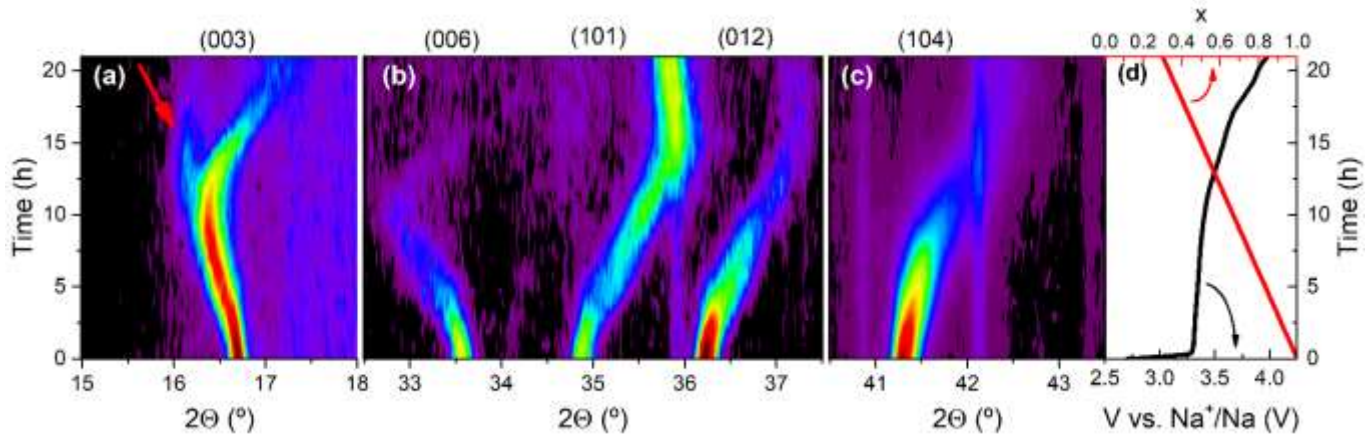

Fig. 5. (a,b,c) 2D representation of the *operando* XRD patterns of *cell 1* for selected 2θ angles of $NaFeO_2$. The cell was charged up to 4.0 V. Reflections are indexed with $R\bar{3}m$ space group. Red arrow in (a) indicates the presence of a secondary phase. (d) Voltage and sodium evolution. Measurement done with Cu K-α source.

suggests that the overpotential reverses the effect of Fe migration, possibly by inducing the migration of at least a proportion of Fe back to the FeO_2 layer, allowing facile sodium diffusion.

By analogy with previous reports of O3 layered oxides based on Fe or Mn,[25,28,47] both the insertion-extraction of sodium and the migration of the transition metal to the sodium plane should have an observable signature in the diffraction patterns of Na_xFeO_2. However, in their recent study of $NaFeO_2$ via an *operando* synchrotron PXRD experiment, Lee *et al.* did not observe any major structural change.[19] In order to resolve this apparent discrepancy and confirm the observation made from the present EIS and PITT measurements, a range of X-ray diffraction experiments were conducted - *in-situ* PXRD measurements using both synchrotron (Figs. S7 and 9(a-c)) and lab scale instruments (Figs. 5, 7 and 9(d-i)), in which *operando* measurements as well as snapshots at specific states of charge were performed. Synchrotron measurements analyse only part of the electrode (typically a few mm^2) and require the current collector to be transparent to X-rays on both sides of the cell due to the transmission geometry of the experiment. Lab-scale measurements are typically performed in Bragg-Brentano reflection mode, allowing the illumination of more than 80% of the electrode with only one transparent current collector required, on the side of the working electrode under study. In this later case a cell developed at CIC Energigune (CICe) has been used, using a transparent rigid Beryllium window,[28,29] which ensures an even pressure over all the electrode's surface as well as a good electrical contact. For the *operando* synchrotron measurements a modified coin cell has been used, with flexible transparent windows (Kapton covered hole) at both sides of the casing, similar to the cell design used by Lee *et al*.[48]

As seen in Fig. S7, the *operando* measurements done at the synchrotron using modified coin cells are similar to the ones reported by Lee *et al.*, with negligible structural change. On the contrary, the occurrence of strong structural changes is revealed by the *operando* measurement using a lab-scale instrument with CICe's beryllium window-based cell, as highlighted by the peaks shifting that can be observed in Figs. 5, 7 and 9(d-f). The fact that this behaviour was not observed in the *operando* synchrotron measurements using modified coin cells is most probably related to the cell design. Indeed, even if the voltage-composition curve of the whole electrode in modified coin cells were very similar to those obtained in a standard coin cell, it is possible that the reaction was strongly delayed in the region of the hole due to lower pressure induced by the flexible Kapton windows.[49,50] It may not have a strong impact in the case of materials presenting good charge-discharge kinetics, but in the case of $NaFeO_2$ the huge charge transfer increase revealed by our EIS measurements when sodium is extracted, most probably prevents a proper homogenization of the electrode state of charge if the pressure is not optimum. The flexible windows, by lowering the cell pressure, decrease the interconnection of the electrode which can delay or even hamper the reaction in the analysed region.

Three experiments were performed using a lab-scale PXRD diffractometer in reflection mode and CICe's custom designed cell with a rigid Beryllium window. First, *cell 1* experienced a single charge in CCCV mode (constant current (CC) corresponding to a rate of C/30 followed by a constant voltage (CV) period of 15 h) up to 4.0 V to observe the structural changes until the end of charge, see Fig. 5. Then, a second cell, *cell 2*, was measured for two cycles, the first in the conservative voltage window 1.0-3.6 V, the second in the extended window 1.0-3.8 V (Fig. 7). For the first cycle the upper voltage limit was increased from 3.5 to 3.6 V to compensate for the greater cell resistance expected in the case of *operando* measurements on powder electrode compared to standard electrochemical testing using laminate electrodes. The discharge voltage has been chosen as low as 1.0 V to compensate for the discharge polarization observed when increasing the charge potential (Fig. S2) and confirmed by the PITT measurements (Fig. 4a). Finally, the experiment of *cell 1* was reproduced using lab-scale PXRD with a third cell, *cell 3*, which after a full charge to 4 V in CCCV mode, followed by 5 days of open circuit relaxation, was measured for a snapshot at the ALBA Synchrotron (Figs. 9(a-c)). It was then discharged in CCCV mode down to 1.5 V (2C constant current, 10h constant voltage), followed by 12 hours open

circuit relaxation, and a snapshot was measured again at the ALBA Synchrotron (see Figs. 9(a-c)). The long relaxation time prior to HRXRD measurement was performed to ensure complete homogenization of the electrode's state of charge and hence avoid the issues encountered with the *operando* measurement in modified coin cells. The overpotential peak observed in Fig. 2a at the beginning of charge at C/10 is not observed in any of the three operando cells, as seen in Figs. 5d, 7c, and 9j. As discussed above, this overpotential peak is a dynamic effect due to an increase of the impedance of the cell. The fact that it is not observed in the operando cells is most probably due to a significantly lower rate of C/30 at which these cells have been run.

The 2D plots of *cell 1* and *cell 3* are presented in Figs. 5 and 9, respectively. The in-plane parameter *a* and interlayer distance for *cell 1* are also presented in Fig. 6b as deduced from Le Bail refinements (see selected patterns in Fig. S8). The pattern evolution for *cell 1* (Fig. 5) and *cell 3* (Fig. 9) showed very similar behaviour during the CCCV charge to 4 V. For both cells a single-phase transformation of the initial O3 phase is observed during the first 10h of the charge. During this period, a shift to lower angles is clearly observed for both cells for the reflections $(00l)_{O3}$, corresponding to an increase of the interlayer distance d_{003} from 5.37 Å to 5.48 Å, as seen in Fig. 6b. During this period, other reflections with contribution from *a* and *b*, such as (101) and (012), shift to higher angles which denotes a shortening of the in-plane cell parameters with Na extraction from 3.02 Å to 2.94 Å, see Fig. 6b. This behaviour has been reported in many compounds with O3 structure and is ascribed to increasing electrostatic repulsion between oxygen atoms (interlayer distance increment) and decrease in the electrostatic repulsion between iron and sodium ions (in-plane distance decrease) when sodium is extracted.[15,28,51,52]

As seen at the vicinity of the $(00l)_{O3}$ reflexions in Figs. 5 and 9, for both *cell 1* and *cell 3* a secondary phase emerges from the initial O3 phase near half charge. It appears at lower diffraction angle, thus corresponding to a greater interlayer distance of 5.58 Å according to the Le Bail refinement of an ex-situ PXRD pattern of an electrode charged to 3.6 V (see Fig. S9 and Table S3). This behaviour is very similar to what has been observed in other O3 TM layered oxides,[15,53] in which a biphasic transformation from O3 to P3 structure is typically observed. The "P" nature of the structure of the secondary phase is ascertained by the (003) and (104) peaks intensity ratio of the P3 phase which are opposite to that of the initial O3 phase, as observed in Fig. S9 and confirmed by the simulations presented in Fig. S10. In the operando measurements of Figs. 5 and 9 the secondary phase is only observed at the vicinity of (00*l*) reflexions, which suggests it is a P3 phase with similar in-plane parameters than the O3 phase. However, in the case of the longer ex-situ measurements of Fig. S9, two small diffraction peaks can be seen close to (104), which suggests a monoclinic distortion of this secondary phase, and thus that it is a P'3 layered structure. This is further confirmed by the Le Bail refinements presented in Fig. S9 using the space groups $R\bar{3}m$ (P3) and $C\,2/m$ (P'3).

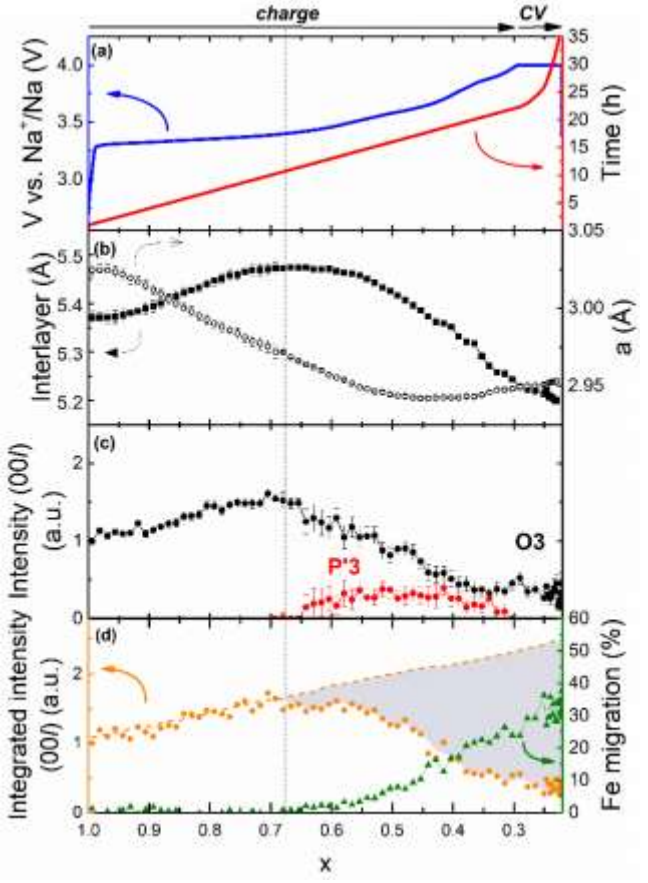

Fig. 6. Analysis of diffracted peak (003) of the *cell 1*, charged to 4.0 V. (a) Voltage profile (blue line) and time (red line) (b) Interlayer distance and cell parameter *a* as obtained from Le Bail refinements of the main O3 phase using $R\bar{3}m$ space group (see examples in Fig. S8). (c) Evolution of the areal intensity of the (003) peaks of the O3 and P'3 phases as deduced from fitting by Pseudo-Voigt functions. (d) Left axis: Normalized total integrated intensity of the (003) reflections (O3 + P'3 phases) from experiment (orange dots) and simulation considering no migration of Fe (discontinuous line). Right axis - percentage of migrated Fe atoms to tetrahedral sites in Na planes (green triangles) deduced from the experimental intensity using equation (S4).

As seen in Figs. 5a, 6b and 9d, at about half charge, when the (00*l*) peaks of the proposed P'3 phase are the more intense, the $(00l)_{O3}$ reflections shift toward higher angles, which indicates a decrease of the interlayer distance of the main phase (O3). For both *cell 1* and *cell 3* this compression of the interlayer distance is continuous until the end of charge, and while this occurs the $(00l)_{O3}$ reflections also lose intensity. The (101), (012) and (104) reflections, which were continuously shifting toward higher angle, start to shift toward lower angle during the second part of the charge. As seen in Fig. 6b, denoting an inflexion from the linear decrease of intra-layer cell parameter $a = b$ observed from x= 0.95 to x= 0.6, and following this inflexion, the *a* parameter marginally increases beyond x = 0.45 to reach 2.94 Å at the end of charge. Additionally, the intensity of the $(00l)_{O3}$ reflection of the main phase starts to decrease. From x= 0.7 to 0.6, this could be ascribed to the O3 → P'3 bi-phasic transition identified above. For lower x values, however, as seen in Fig. 5a the intensity of the (00*l*) reflections of both O3 and P'3 phases decrease, demonstrating that another factor must be taken into account. This decrease of intensity is observed in all reflections,

except (101) which has the least contribution from *c*. In consequence, this suggests a reduction of the contrast in the *c* direction, which is a first indication of possible iron migration to the sodium layer sites as proposed by previous studies for $NaFeO_2$.[15,19,20] In addition, iron migration is also expected to induce a contraction of the interlayer distance, due to a reduction of the electrostatic repulsion between oxygen-oxygen atoms,[15,18,54] which is in agreement with the (00*l*) peaks evolution observed here. Finally, Li *et al.*, reported a direct observation from HRTEM of a high degree of iron migration in a $NaFeO_2$ electrode material charged to 4.5 V, which presented an interlayer distance of 4.893 Å and an in-plane distance of 2.9856 Å.[15] This confirms that contraction of the interlayer distance concomitant with expansion of the in-plane distance are both indication of iron migration. The fact that the intensity of both O3 and P'3 (00*l*) reflections decrease during the second part of the charge in *cell 1* and *cell 3* suggests that both phases suffer from Fe migration toward the Na layers. Furthermore, the P'3 phase becomes undetectable beyond 3.8 V (x = 0.3, t = 20 h) in the *operando* measurements of both *cell 1* and *cell 3*, as seen in Figs. 5a and 9d, while the O3 phase is still observed. This suggests that the iron migration hinders the evolution of the O3 → P'3 transition, probably due to kinetic limitation related to degraded Na mass diffusion.

A similar behaviour is observed in Fig. 7 for *cell 2* upon charge with an increase in interlayer distance and the appearance of a secondary phase at x = 0.67 (t ≈ 10 h and 55h during the first and second charge, respectively). From 3.3 V to 3.6 V during the first charge the $(003)_{O3}$ peak shifts to larger angles indicating a contraction of the interlayer distance similar to what has been observed for *cell 1* and *cell 3*, with an associated loss of intensity indicative of iron migration. When the cell is further discharged from 3.6 V, the $(003)_{O3}$ peak position initiates a low angle shift. This denotes an increase of the interlayer distance up to about half discharge accompanied by an increase in intensity, suggesting that the charge reaction is inverted, i.e. that iron seems to initiate a migration back to the metal-oxide layers while sodium is being inserted. However, before reaching the position it showed at 3.3 V during charge, the $(003)_{O3}$ peak shifts back to higher 2θ values reaching a position close to the initial value during the second half of the discharge, but with a lower intensity. This suggests that sodium intercalation inverts the interlayer distance evolution towards contraction while iron is still present in the Na layers, which may indicate that iron back-migration is kinetically disfavoured compared to sodium intercalation. Concerning the reflections with strong in-plane lattice contribution (101) and (012), they present a symmetric behaviour during charge and discharge: *a* and *b* lattice parameters shrink almost linearly with Na extraction and increase quasi-linearly with insertion (Fig. 7). The intensity loss during charge in the (012) reflection is nearly recovered upon discharge from 3.6 V. On the other hand, the (003) reflection with only interlayer distance contribution follow a different path during charge and discharge processes at the first cycle. During the 1V constant voltage (CV) periods at the end of the first and second discharges of *cell 2* no significant changes can be observed. The second charge of *cell 2* is very similar to the first one up to 3.6 V, although the shift to lower 2θ values of the $(00l)_{O3}$ peaks and the appearance of the secondary P'3 phase is less pronounced. This is probably due to the fact that some iron remains in the sodium layers, being a second indication that iron migration hinders the evolution of the P'3 phase. The reflections (101) and (012) show a change in their shift trend above ≈ 3.6 V for both *cell 1* and the second cycle of *cell 2*, together with an intensity increase for (101). This is an indicator that the main charge mechanism has changed. Moreover, the discharge is less reversible when discharged from 3.8 V compared to the first cycle, as the (003) reflection only slightly shifts back to lower angles while its intensity remains low, similar to the (012) reflection, whose intensity is only slightly

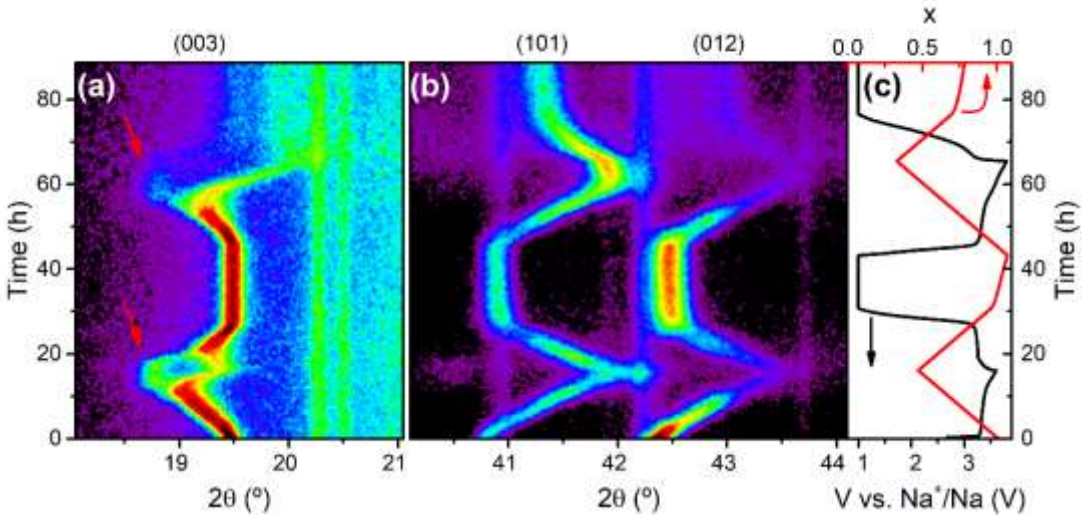

Fig. 7. (a,b,c) 2D representation of *operando* XRD patterns of *cell 2* for selected 2θ angles. The cell was first cycled in the voltage range of V = 3.6-1.0 V, hold at 1.0 V until C/300 current was reached (806 μA g^{-1}) and then in the voltage range V = 3.8-1.0 V. Reflections are indexed with $R\bar{3}m$ space group. Red arrows indicate the presence of a secondary phase. (c) Voltage and sodium content evolution are shown in the right panel. Measurement done with Co K-α source.

recovered. At the end of discharge and during the 1V CV period, it appears clearly that, although there is some degree of structural reversibility, the reflections have not reached their original positions or intensities, that is, the original pristine structure is not recovered. This suggests that there is a threshold voltage near 3.6 V above which the structural transformation as well as the amount of inserted sodium is poorly reversible, in accordance with the electrochemical performance degradation observed increasing the charge voltage in Figs. 2b, 4a and S2.

According to previous reports, it is expected that this irreversibility of the Na extraction in $NaFeO_2$ upon charge to be closely related to a change of the Fe occupancy due to its migration toward the Na layers. Occupancy determination requires Rietveld refinement of diffraction patterns. However, limited angular range is a typical restriction of *operando* lab-scale PXRD measurements that prevents Rietveld analysis, such as in the case of *cells 1*, *2* and *3*. Even in the case of the ex-situ measurement of Fig. S9 performed at 3.6V with extended angular range and large acquisition time, Rietveld refinement is not feasible due to the overlap and weakness of most of the O3 and P'3 phases' reflections, especially above 60° where they are overwhelmed by the background signal and the reflections from current collector and sample holder. Fe migration is however qualitatively confirmed at 4 V in Fig. S11, in which the intensity ratio between the (003) and (101) reflections is closer to simulated pattern considering 30% of TM migration.

Owing to the strong anisotropy of the layered structure, further insight into the occupancy evolution in the stacking direction can be achieved by looking at the evolution of the intensity of the (003) reflection. For that purpose, simulations of the dependence of the (003) reflexion intensity with sodium content, Fe occupancy and cell parameters have been performed using the FullProf suite software ,[27] assuming that the $R\overline{3}m$ space group describes the predominant phases at all states of charge. The intensity dependence on the percentage of Fe migration z has been further parametrized using a polynomial function, in order to be able to estimate the theoretical intensity evolution versus cell parameters and Na content for z =0, as well as estimating the amount of Fe migration from the measured intensity evolution. More details on the method can be found in supplementary information (Fig. S12).

In Figs. 6d (*cell 1*) and 8b (*cell 3*), the theoretically expected intensity for the (003) reflection in the space group $R\overline{3}m$ has been plotted (dashed line) taking into account the cell parameters deduced from Le Bail refinements of diffraction data, the sodium content deduced from the electrochemical measurement, and considering no Fe migration (i.e. using equations S4 or S5 with z = 0). For both *cell 1* and *cell 2*, there is a very good match between theoretical curve (dashed line, orange online) and experimental data (plain circles, orange online) for the evolution of the (003) peak intensity with Na removal until x ≈ 0.64 (that is 3.5 V and 3.4 V for *cell 1* and *cell 2*, respectively). This indicates that until that point no other change of occupancy occurs than that of Na. Beyond that point, the measured peak intensity departs from the theoretical

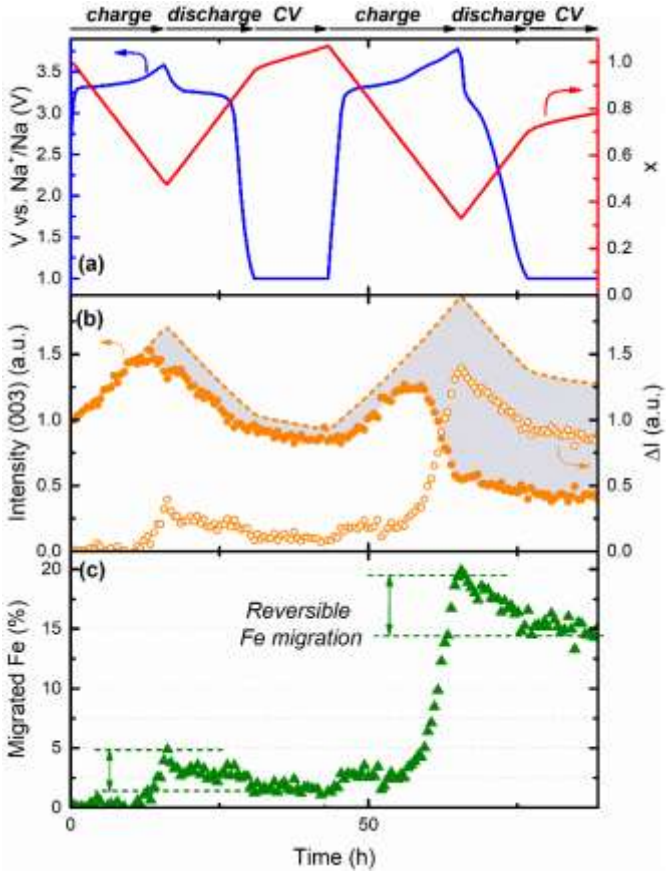

Fig. 8. Analysis of the interlayer reflection (003) versus time for *cell 2* during the operando PXRD measurement presented in Fig. 7. (a) Cell voltage and sodium content evolution. (b) Left axis: Normalized experimental (orange plain circles) and theoretical (orange discontinuous line) intensity of the (003) reflection. The experimental intensity has been corrected for Lorentz-Polarization factor, absorption, sample volume and thermal factor (see ESI Table 4 for more details). The theoretical intensity has been calculated from equation S4 assuming no migration of Fe (z = 0). Right axis: difference between theoretical and experimental intensities (orange open circles). (c) Percentage z of migrated Fe to tetrahedral sites in Na planes based on equation S4.

dashed line, indicating thus the onset of a change of the occupancies (see Figs.6d and 8b). The difference ΔI between theoretical and experimental normalized intensities of *cell 2* has been plotted in the right vertical axis of Fig. 8b. It can be clearly seen from this plot that the evolution of ΔI is mainly reversible upon discharge after charge to 3.6 V as 90% of the initial intensity is recovered at the end of discharge. This suggests that the occupancy change that occurs upon charge beyond ≈ 3.4 V (x = 0.64) is actually a reversible process. During the second charge the divergence of the experimental intensity from the theoretical one is strongly increased beyond 3.6V, and the reversibility of this loss of intensity is only partial upon discharge from 3.8 V as only 40% of the initial intensity is recovered at the end of the second discharge.

As pointed out by Kubota *et al.* for $NaCrO_2$, two possible sites are available in the O3 structure for Fe migration into the inter-slabs: Na sites (octahedral sites) or tetrahedral sites.[18] Simulations for the two types of Fe migration in $Na_{0.6}FeO_2$ are presented in Fig. S13 at the vicinity of the (101) reflexion and considering 40% Fe migration to the inters-labs. A clear

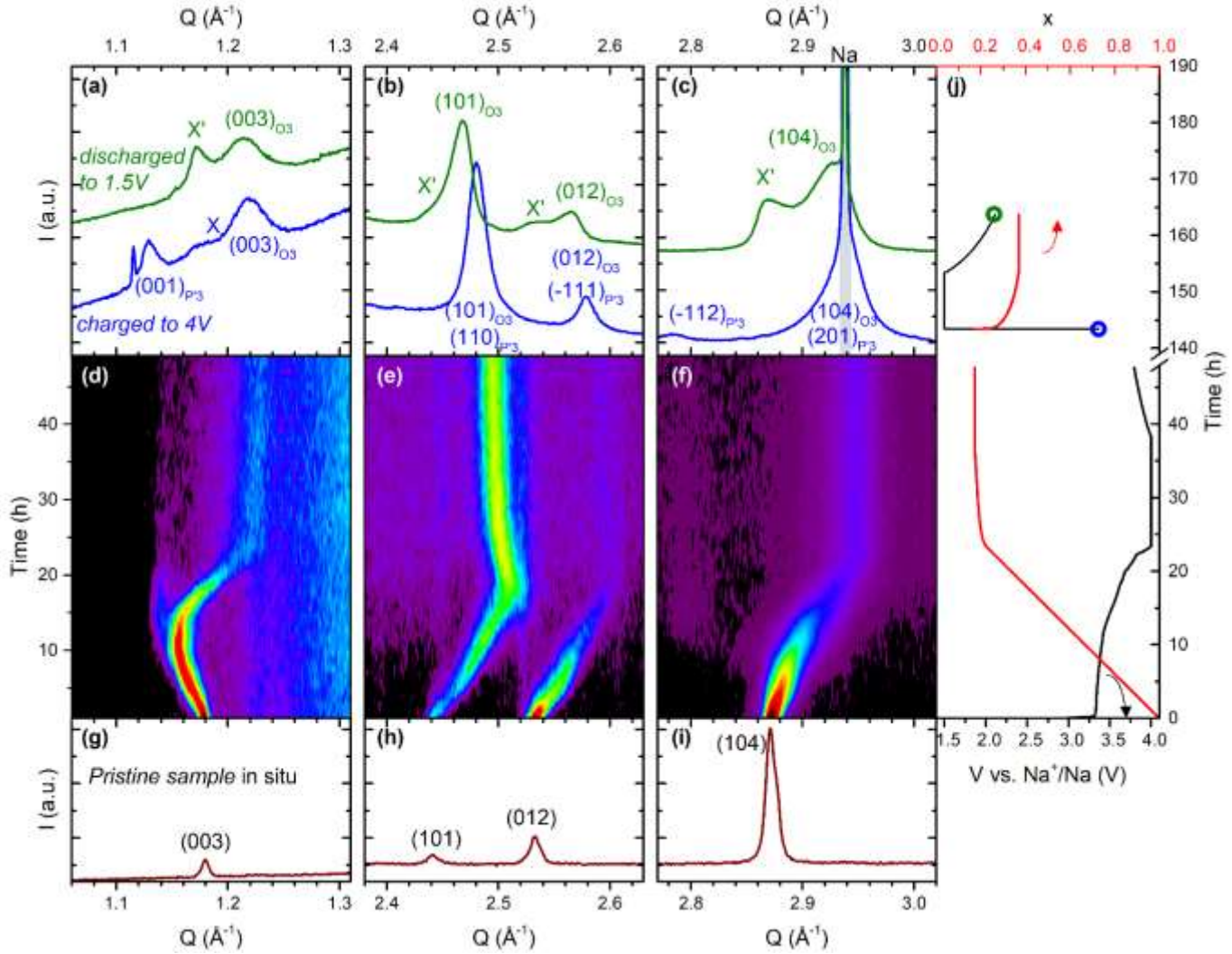

Fig 9. XRD patterns of *cell 3* for selected angle ranges. (a,b,c) HRXRD patterns recorded at ALBA synchrotron at charged to 4 V (blue,1) and discharged to 1.5 V (green,2) states. Na reflection is shaded in gray in panel (c). (d,e,f) *Operando* PXRD 2D data plots recorded at CIC Energigune. (g,h,i) *In situ* PXRD measured at CIC Energigune of pristine material. Reflections are indexed as $R\bar{3}m$ and *C 2/*m space groups, for O3 and P'3 phases respectively. A third phase, named as "X", is visible in charged and discharged states. Note that metallic Na reflection is only visible in patterns taken at ALBA synchrotron in panel (c) due to the transmission geometry used, as opposed to reflection geometry in other measurements. (j) Voltage profile and sodium content as a function of time. Points at which HRXRD patterns were taken are marked.

difference in the intensity relation of reflections (101) and (012) can be observed from Fig. S13 depending on the site to which Fe migrates. From the operando XRD patterns evolution at the end of charge of *cell 1*, see e.g. S8, in which the (101) reflection is clearly more intense than the (012) reflection, it can be concluded that Fe migrates essentially to the tetrahedral sites. The amount of Fe migration z to tetrahedral sites in Na planes deduced from the evolution of the normalized experimental intensity of the interlayer reflection (003) of Fig. 6d and 8b using equation S4 is presented in Figs. 6d and 8c (green triangles) for *cell 1* and *cell 2*, respectively. It appears clearly that the amount of migrated Fe is negligible below 3.4V (x = 0.6), and increases linearly at higher potential to reach 25% and 5%, respectively, for *cell 1* charged to 4 V and *cell 2* charged to 3.6 V. This percentage is further increased to 20% for *cell 2* charged to 3.8 V and 40% in *cell 1* after holding 4 V over 15 hours. Interestingly, this iron migration in *cell 2* appears mainly reversible when discharged down to 1.0 V from 3.6V, as 90% of the initial intensity is recovered. This confirms the observation previously made from Fig. 7. The fact that the intensity is not totally recovered while the Na insertion appears complete suggests that some iron remains migrated into the Na layers at the end of the first discharge from 3.6 V, and that Na ions possibly occupy the corresponding vacancies in the metal-oxide layers. During the second cycle of *cell 2* a fast increment of migrated Fe can be seen beyond 3.6 V (t = 60 h), when an inflection in the shift of (101) and (012) reflections can be seen in Fig. 7, reaching 20% of the total Fe at 3.8V. Upon the next discharge the intensity recovery corresponds to only ≈ 25 % of migrated Fe returning to the FeO_2 layers, which is probably overestimated if one considers the possibility of Na occupancy into the TM layers' vacancies. This reveals that the charge voltage has a strong influence on the reversibility of the Fe migration. The influence of the site to which Fe is considered to migrate on the amount of Fe migrated deduced from equations (S4) and (S5) can be appreciated in Fig. S14 for *cell 1 and cell 2*. Although

there is a difference in the estimated amount of Fe migration of about 13%, the evolution of the Fe migration upon cycling appears totally independent to the inter-slab site to which Fe is considered to migrate.

In order to evaluate the degree of reversibility of the transformations observed upon charge beyond 3.8 V, *cell 3* has been further discharged from 4V to 1.5 V in CCCV mode. As seen in Fig. 9(a-c) the peaks of the O3 phase have all shifted toward lower angle when *cell 3* has been discharged from 4 V (blue online) to 1.5 V (green online). This, and the fact that a sodium content of about 0.2 has been re-intercalated upon discharge to 1.5 V, strongly suggests that the iron migration and sodium extraction are actually still partially reversible even in a deeply deintercalated Na_xFeO_2 material, in accordance with the results of the PITT analysis, although in lower extend compared to *cell 2* discharged from 3.6 and 3.8 V.

Interestingly, although in the 2D plots of Figs. 5 and 9 the $(00l)_{P'3}$ peaks of the P'3 phase seem to have totally disappeared when charged to 4 V, $(001)_{P'3}$ is clearly visible in the synchrotron measurement made 30 h later (Fig. 9a). Fig. S15 compares a 66h lab-scale measurement of *cell 3* charged to 4V (accumulation of 33 single measurements of 2h), a single 2h lab scale measurement and the synchrotron measurement of the same *cell 3* at the same state of charge but performed after a few days of OCV relaxation. It appears clearly from Fig. S15 that the (00*l*) peak corresponding to the P'3 phase was actually present in the lab-scale measurement at Q ≈ 1.13 $Å^{-1}$, although its intensity was too low to be properly observed with a single 2h acquisition time. Comparing the 66h lab-scale acquisition with the synchrotron measurement, it appears also clear that the intensity of the (00*l*) peak of the P'3 phase has increased, suggesting that the O3→P'3 transition corresponds to the thermodynamic equilibrium transformation path, and that the P'3 phase disappearance observed *operando* at the end of charge was a dynamic induced effect probably related to kinetic limitations due to Fe migration. Such kinetic effect may also be at origin of the discrepancy between the PITT experiment, which is expected to be closer to the equilibrium path and suggests a biphasic transition at the voltage plateau observed at 3.3V, and the operando XRD experiments of *cells 1*, *2* and *3* in which the O3→P'3 biphasic transition is not observed until 3.45 V.

A third peak is also observed around 1.17 $Å^{-1}$ in the synchrotron measurement, half-way between the (00*l*) peaks of the P'3 (Q ≈ 1.13 $Å^{-1}$) and O3 phases (Q ≈ 1.22 $Å^{-1}$). Even though the position of this peak is very close to the (003) peak of the pristine O3 structure (see. Fig. 9), the absence of pristine phase's reflections at higher angles confirms it is a new phase and not unreacted material, indicating that 3 phases are present when charged to 4 V. A third unidentified phase, cohabitating with O3 and P'3 phases, was also observed upon charge in O3-$Na_{0.77}Fe_{2/3}Mn_{1/3}O_2$ by Mortemard de Boisse *et al.* near 4 V,[53] and a three phases state were also reported for charged O3-$Na_{2/3}Fe_{2/3}Mn_{1/3}O_2$ by *Gonzalo et al.*.[28] In O3-$Na_{0.77}Fe_{2/3}Mn_{1/3}O_2$ charged beyond 4 V, reaching near total sodium removal (x_{Na} = 0.16), Mortemard de Boisse *et al.* have shown that this third unidentified phase, which they labelled "X", was the only phase present, suggesting that both O3 and P'3 phases transformed and merged into this unidentified phase. The authors suggested this transition to occur via stacking faults and layer gliding. They found similarities of this unknown phase with the low crystallinity phase observed at low Na intercalation content in P2-$Na_{0.62}Mn_{1/2}Fe_{1/2}O_2$ and P2-$Na_{2/3}Mn_{2/3}Ni_{1/3}O_2$,[55,56] for which a transition toward an O2 phase via layer gliding was proposed. In these previous reports as well as in the present study, the low crystallinity of the deintercalated phase prevents Rietveld refinement to undoubtedly confirm its real nature. This research work eventually sheds a new light on this puzzling question, as it suggests that, beyond layer gliding and stacking faults occurrence related to sodium depletion, the nature of the de-intercalated phase of sodium TM layered oxides appears intimately related with TM migration toward the Na layers. TM migration is known to block Na diffusion as well as inducing covalent layer-to layer bonds that prevent layer gliding.[16,18] It is thus not surprising that a high amount of migrated TM leads to a highly disordered phase with a low degree of crystallinity, as the structure loses the plasticity and mobility required to allow a long range order to establish. An *ex-situ* XRD measurement was done on an electrode charged to 4.5 V, in order to get a hint on the nature of the "X" phase (Fig. S16). First of all, it can be observed from Fig. S16 that at 4.5 V the material presents a phase coexistence of O3 and "X" phase, while the reflection of the P'3 phase have disappeared, including the peaks related to the monoclinic distortion. This confirms that Fe migration hampers the O3 → P'3 transformation, and that the O3 phase does not present appreciable monoclinic distortion, contrary to what was observed for $NaCrO_2$ by Kubota et al..[18] Moreover, broad diffraction peaks can be observed at low angles near Q = 1.77 $Å^{-1}$ which suggests that the "X" phase is not a layered phase. This is in agreement with the observation of spinel-like local arrangement in $NaFeO_2$ charged to 4.5 V reported by Li et al. from transmission electron microscopy.[15] However, the very low crystallinity of the phase, inducing broad and weak reflections, prevents a proper refinement of the structure.

The phase evolution observed in $NaFeO_2$ upon charge and discharge is summarized in Fig. 10. It appears to be qualitatively very similar to what has been previously observed in other O3 layered oxides, especially the O3-$Na_{0.77}Fe_{2/3}Mn_{1/3}O_2$ phase reported by Mortemard de Boisse *et al.*. It starts by a single phase solid solution region of the initial O3 phase for 1 > x > 0.7, followed by a biphasic transformation O3 → P'3 for x > 0.7. Concomitantly, Fe starts migrating to the inter-slab near x = 0.65, which seems to affect the evolution of the O3 → P'3 phase transition. Finally, beyond x = 0.4 both P´3 and O3 phases seem to merge in a new unidentified non-layered "X" phase, and Fe migration becomes less and less reversible as the charge voltage increases, which is traduced by an increasing overpotential upon discharge. This suggests that the layered structure is a requisite for the reversibility of Fe migration.

Apart from the slight monoclinic distortion of the P'3 phase, the two main differences between $NaFeO_2$ and other O3 layered oxides seems to be that i) TM migration occurs before the O3 to P3 transition is completed, and ii) the overpotential needed to

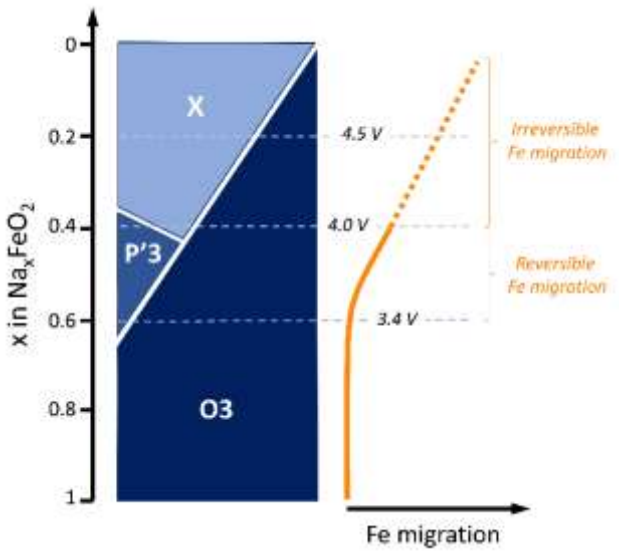

Fig. 10. Scheme of phase evolution and iron migration upon sodium extraction in Na_xFeO_2.

move iron back to its initial position upon discharge is larger, limits the discharge reaction in normal cycling conditions.

The general consensus in the previously reported work is that tetrahedral sites need to be available in the Na layers for TM to migrate.[3,15,57] This implies that TM may occur in O phases, but is prevented in P phases due to the absence of tetrahedral sites. This explains why, when the initial phase is P, or if the O to P transition upon charge is complete before TM migration occurs, higher state of charge can be achieved before TM occurs.

It had been proposed that Na_xFeO_2 was particularly prone to Fe migration because O3 to P3 transition had not been observed for this material contrary to other O3 layered oxides that show a complete O3 to P3 transition before any sign of TM migration can be detected.[3] Here the onset of an O3 to P'3 transition is actually demonstrated, which suggests that the origin of the more pronounced TM migration in Na_xFeO_2 is related to the intrinsic properties of the O3-Na_xFeO_2 phase. As a matter of fact, various explanations have been discussed in the literature for the spontaneous migration of Fe into the Na layers, such as the local concentration of neighbour Fe,[15] the assistance of Jahn Teller effect of high spin Fe^{4+},[15] as well as Na vacancies concentration.[3,57] It seems thus reasonable to conclude that it is the sooner occurrence of TM migration in $NaFeO_2$ that prevents the complete evolution of the O to P transition upon charge. Thereby, such as the sooner occurrence of TM migration in $NaFeO_2$ upon charge, the large overpotential needed to induce back migration upon discharge is probably related to the intrinsic properties of the O3-Na_xFeO_2 phase.

It is expected that the monoclinic distortion of the P'3 phase compared to the P3 phase does not affect the geometry of the sites in the Na layers, that is, only prismatic sites are available so that Fe migrating is not expected to occur in this phase similarly to the P3 phase observed in other O3 TM layered oxides. A possible explanation of the observed effect of TM migration on the disappearance of the P'3 phase observed operando when charged to compositions $x < 0.3$ could be related to a P to O transition of the P'3 phase, hence allowing Fe migration. Transition from P3 to O3 is actually quite common for O3 TM oxides at the end of charge. Such transition is not detected in the operando as well as ex-situ patterns presented here (see Figs. 5 and 9(a-f)), which suggests that it might occur in the form of stacking faults rather than nucleation and growth of new O phase domains.

When the amount of migrated iron is large at the end of charge, like in the case of *cell 1* charged to 4V or the second cycle of *cell 2* charged to 3.8 V, sodium insertion is not allowed unless a very high overpotential is applied. When the amount of migrated iron is low, like in first cycle of *cell 2* charged to 3.6 V, Na appears to be allowed to reinsert with a negligible overpotential. This suggests that there is a threshold percentage of migrated Fe below which Na diffusion is only marginally affected. This is probably related to the evolution of the "X" phase, which might become thermodynamically more stable than the layered structure when the Fe migration passes a certain threshold, preventing the reversibility of the reaction. However, even when Na is allowed to reinsert with negligible overpotential, a portion of the migrated iron stays in the Na layers, leading to a progressive increase of migrated Fe upon cycling as observed in *cell 2*. This is probably the main source of capacity fading in $NaFeO_2$, and possibly of other layered oxides in which TM migration occur.

The present study allows to directly correlate the onset of TM migration with the shrinking of the interlayer distance, confirming the statement made by Li et al. that the latter is indicative of the former.[15] Indeed, in absence of any change of TM occupation, Na extraction is expected to increase the interlayer distance due to electrostatic repulsion, so that interlayer distance contraction upon charge appears indeed as a solid indicator of the occurrence of TM migration. Contraction of the interlayer distance at the end of charge is actually common for a large range of O3 as well as P2 layered structures,[15,53,57–59] including of binary or ternary compounds known for their superior performance, and it has also been reported in lithium-ion layered oxides.[35,55,57–60] As a matter of fact, this contraction systematically occurs when an O phase is present at the end of charge. However, the onset of TM migration as well as its quantification is rarely documented, probably due to the reduction of crystallinity that this phenomenon induces which prevents Rietveld analysis. The partial reversibility of the extraction-insertion of Na in Na_xFeO_2 in presence of migrated TM, which appears to be directly related to the ability of TM to migrate back of the TM layers upon insertion, is an unexpected result in view of the large literature available in conventional $(Na,Li)_xTMO_2$ layered oxides. Recent publications dealing with Li-rich TM layered oxides have however revealed reversible TM migration of the alkali metal planes at intermediate state of charge, which suggests that this phenomenon has probably be overlooked for conventional TM layered oxides.[23,61,62]

Conclusions

In summary, pure O3-$NaFeO_2$ layered structure was synthesized and its structural and kinetic properties studied by means of *in-situ/operando* XRD, EIS and PITT. The charge reaction in $NaFeO_2$ appeared very similar to other O3 TM oxides, initiating by a solid-solution with expansion of the interlayer distance until a sodium content of $x \approx 0.7$ is reached, followed by a bi-phasic transformation from O3 to P'3 beyond that point. The discrepancy of these results with those of Lee *et al.* which reported negligible changes of the main phase has been ascribed to differences in the *in-situ* cell design, $NaFeO_2$ being much more sensitive to this factor than other materials.

Three indicators revealed the migration of Fe upon charge above $x \approx 0.5$ (3.5 V) in the main O3 phase: i) a strong decrease of the intensity of the (00*l*) reflexions, ii) a contraction of the interlayer distance of the main O3 phase and iii) an increase of the intra-layer distance. By quantitatively interpreting the loss of intensity of the (003) reflexion in terms of Fe migration it has been found that 40% of the initial iron migrated to the Na layers at the end of charge to 4 V. The reduction in reflection intensity of the proposed P'3 phase suggest that the O3 to P'3 transition is prevented by Fe migration, probably due to kinetic limitation induced by the this later. A long relaxation time at charged state, however, allows the growth of the P'3 phase, which suggests that the presence of a P'3 phase when charged to 4 V corresponds to thermodynamic equilibrium.

Surprisingly, *in-situ* XRD upon discharge strongly suggests that Fe migration in $NaFeO_2$ is partially reversible, which has been confirmed by PITT measurements revealing unaffected sodium diffusion coefficient upon insertion even when discharged from 4 V. However, this partial reversibility is at the cost of a high over-polarization which has been assigned to the electromotive force needed to move iron atoms back to their original positions, which is reflected in an increase of several orders of magnitude of the charge transfer resistance in EIS measurements. The degree of reversibility decreases while the charge potential increases, which seems to be correlated to the apparition of an unknown non-layered "X" phase.

The similarities of the XRD pattern evolution of Na_xFeO_2 at the end of charge with what has been previously reported for other TM layered oxide compositions confirms that TM migration is possibly the major source of electrochemical performance degradation when too high alkali metal deintercalation levels are reached. The present report of reversible TM migration in $NaFeO_2$, a material reputed for the dramatic degradation that this phenomenon induces on its performance, suggests that beyond limiting the occurrence of TM migration, the identification and control of the factors that allow its reversibility could pave the way for the development of new strategies for TM layered oxides optimization.

Conflicts of interest

There are no conflicts to declare.

Acknowledgements

Authors acknowledge the financial support of the Ministerio de Economía y Competitividad through the project ENE2016-75242-R and the Australian Research Council via DE160100237 / DP170100269. The authors would also like to thank the Basque Government for financial support through ELKARTEK project CICE17. B. Silván thanks CIC Energigune for the Ph.D. Scholarship. Finally, the Authors acknowledge M. Jauregui, B. Acebedo, B. Orayech, M. Reynaud and M. Casas-Cabanas for fruitful scientific discussion. Part of this research was undertaken on the Powder Diffraction beamline at the Australian Synchrotron, part of ANSTO and at the Materials Science and Powder Diffraction beamline at ALBA Synchrotron with the collaboration of ALBA staff.

1 G. Martin, L. Rentsch, M. Höck and M. Bertau, *Energy Storage Mater.*, 2017, **6**, 171–179.
2 V. Palomares, M. Casas-Cabanas, E. Castillo-Martínez, M. H. Han and T. Rojo, *Energy Environ. Sci.*, 2013, **6**, 2312.
3 N. Yabuuchi, K. Kubota, M. Dahbi and S. Komaba, *Chem. Rev.*, 2014, **114**, 11636–11682.
4 M. D. Slater, D. Kim, E. Lee and C. S. Johnson, *Adv. Funct. Mater.*, 2013, **23**, 947–958.
5 P. K. Nayak, L. Yang, W. Brehm and P. Adelhelm, *Angew. Chem. Int. Ed.*, 2018, **57**, 102--120.
6 M. S. Islam and C. A. J. Fisher, *Chem Soc Rev*, 2014, **43**, 185–204.
7 S. P. Ong, V. L. Chevrier, G. Hautier, A. Jain, C. Moore, S. Kim, X. Ma and G. Ceder, *Energy Environ. Sci.*, 2011, **4**, 3680.
8 J. W. Choi and D. Aurbach, *Nat. Rev. Mater.*, 2016, **1**, 16013.
9 N. Ortiz-Vitoriano, N. E. Drewett, E. Gonzalo and T. Rojo, *Energy Env. Sci*, , DOI:10.1039/C7EE00566K.
10 X. Xiang, K. Zhang and J. Chen, *Adv. Mater.*, 2015, **27**, 5343–5364.
11 M. H. Han, E. Gonzalo, G. Singh and T. Rojo, *Energy Env. Sci*, 2015, **8**, 81–102.
12 C. Delmas, C. Fouassier and P. Hagenmuller, *Phys. B*, 1980, **99**, 81–85.
13 J. Martinez De Ilarduya, L. Otaegui, J. M. López del Amo, M. Armand and G. Singh, *J. Power Sources*, 2017, **337**, 197–203.
14 B. Zhang, R. Dugas, G. Rousse, P. Rozier, A. M. Abakumov and J.-M. Tarascon, *Nat. Commun.*, 2016, **7**, 10308.
15 X. Li, Y. Wang, D. Wu, L. Liu, S.-H. Bo and G. Ceder, *Chem. Mater.*, 2016, **28**, 6575–6583.
16 S.-H. Bo, X. Li, A. J. Toumar and G. Ceder, *Chem. Mater.*, 2016, **28**, 1419–1429.
17 D. Mohanty, J. Li, D. P. Abraham, A. Huq, E. A. Payzant, D. L. Wood and C. Daniel, *Chem. Mater.*, 2014, **26**, 6272–6280.
18 K. Kubota, I. Ikeuchi, T. Nakayama, C. Takei, N. Yabuuchi, H. Shiiba, M. Nakayama and S. Komaba, *J. Phys. Chem. C*, 2015, **119**, 166–175.
19 E. Lee, D. E. Brown, E. E. Alp, Y. Ren, J. Lu, J.-J. Woo and C. S. Johnson, *Chem. Mater.*, 2015, **27**, 6755–6764.
20 N. Yabuuchi, H. Yoshida and S. Komaba, *Electrochemistry*, 2012, **80**, 716–719.
21 J. S. Thorne, S. Chowdhury, R. A. Dunlap and M. N. Obrovac, *J. Electrochem. Soc.*, 2014, **161**, A1801–A1805.
22 Y.-T. Zhou, X. Sun, B.-K. Zou, J.-Y. Liao, Z.-Y. Wen and C.-H. Chen, *Electrochimica Acta*, 2016, **213**, 496–503.
23 M. Sathiya, K. Hemalatha, K. Ramesha, J.-M. Tarascon and A. S. Prakash, *Chem. Mater.*, 2012, **24**, 1846–1853.

24 J. Billaud, G. Singh, A. R. Armstrong, E. Gonzalo, V. Roddatis, M. Armand, T. Rojo and P. G. Bruce, *Energy Environ. Sci.*, 2014, **7**, 1387.
25 X. Li, D. Wu, Y.-N. Zhou, L. Liu, X.-Q. Yang and G. Ceder, *Electrochem. Commun.*, 2014, **49**, 51–54.
26 E. A. Olivetti, G. Ceder, G. G. Gaustad and X. Fu, *Joule*, 2017, **1**, 229–243.
27 J. Rodríguez-Carvajal, *Phys. B Condens. Matter*, 1993, **192**, 55–69.
28 E. Gonzalo, M. H. Han, J. M. López del Amo, B. Acebedo, M. Casas-Cabanas and T. Rojo, *J Mater Chem A*, 2014, **2**, 18523–18530.
29 M. H. Han, E. Gonzalo, M. Casas-Cabanas and T. Rojo, *J. Power Sources*, 2014, **258**, 266–271.
30 F. Fauth, I. Peral, C. Popescu and M. Knapp, *Powder Diffr.*, 2013, **28**, S360–S370.
31 F. Fauth, R. Boer, F. Gil-Ortiz, C. Popescu, O. Vallcorba, I. Peral, D. Fullà, J. Benach and J. Juanhuix, *Eur. Phys. J. Plus*, 2015, **130**, 160.
32 K. S. Wallwork, B. J. Kennedy and D. Wang, *AIP Conf. Proc.*, 2007, **879**, 879--882.
33 R. G. Haverkamp and K. S. Wallwork, *J Synchrotron Rad*, 2009, **16**, 849.
34 B. Schmitt, C. Bronnimann, E. F. Eikenberry, F. Gozzo, C. Horrmann, R. Horisberger and B. Patterson, *Nucl. Instrum. Methods Phys. Res. A*, 2003, **501**, 267--272.
35 R. J. Gummow, N. Sharma, R. Feng, G. Han and Y. He, *J. Electrochem. Soc.*, 2013, **160**, A1856–A1862.
36 N. Sharma, P. Serras, V. Palomares, H. E. A. Brand, J. Alonso, P. Kubiak, M. L. Fdez-Gubieda and T. Rojo, *Chem. Mater.*, 2014, **26**, 3391–3402.
37 M. D. Levi and D. Aurbach, *J. Phys. Chem. B*, 1997, **101**, 4641–4647.
38 C. Ho, I. D. Raistrick and R. A. Huggins, *J. Electrochem. Soc.*, 1980, **127**, 343–350.
39 C. J. Wen, B. A. Boukamp, R. A. Huggins and W. Weppner, *J. Electrochem. Soc.*, 1979, **126**, 2258--2266.
40 J. Zhao, L. Zhao, N. Dimov, S. Okada and T. Nishida, *J. Electrochem. Soc.*, 2013, **160**, A3077–A3081.
41 Y. Takeda, K. Nakahara, M. Nishijima, N. Imanishi and O. Yamamoto, *Mater. Res. Bull.*, 1994, **29**, 659–666.
42 A. S. Aricò, P. Bruce, B. Scrosati, J.-M. Tarascon and W. van Schalkwijk, *Nat. Mater.*, 2005, **4**, 366–377.
43 J. S. Thorne, R. A. Dunlap and M. N. Obrovac, *J. Electrochem. Soc.*, 2013, **160**, A361–A367.
44 A. Lasia, *Electrochemical Impedance Spectroscopy and its Applications*, Springer - Verlag New York, 1st edn., 2014.
45 E. Barsoukov and J. R. Macdonald, Eds., *Impedance spectroscopy: theory, experiment, and applications*, Wiley-Interscience, Hoboken, N.J, 2nd ed., 2005.
46 Y. Zhu and C. Wang, *J. Phys. Chem. C*, 2010, **114**, 2830–2841.
47 N. Sharma, O. K. A. Bahri, M. H. Han, E. Gonzalo, J. C. Pramudita and T. Rojo, *Electrochimica Acta*, 2016, **203**, 189–197.
48 E. Lee, J. Lu, Y. Ren, X. Luo, X. Zhang, J. Wen, D. Miller, A. DeWahl, S. Hackney, B. Key, D. Kim, M. D. Slater and C. S. Johnson, *Adv. Energy Mater.*, 2014, **4**, 1400458.
49 G. Ouvrard, M. Zerrouki, P. Soudan, B. Lestriez, C. Masquelier, M. Morcrette, S. Hamelet, S. Belin, A. M. Flank and F. Baudelet, *J. Power Sources*, 2013, **229**, 16–21.
50 O. J. Borkiewicz, K. M. Wiaderek, P. J. Chupas and K. W. Chapman, *J. Phys. Chem. Lett.*, 2015, **6**, 2081–2085.
51 J. N. Reimers and J. R. Dahn, *J. Electrochem. Soc.*, 1992, **139**, 2091–2097.
52 K. Kubota, T. Asari, H. Yoshida, N. Yaabuuchi, H. Shiiba, M. Nakayama and S. Komaba, *Adv. Funct. Mater.*, , DOI:10.1002/adfm.201601292.
53 B. Mortemard de Boisse, J.-H. Cheng, D. Carlier, M. Guignard, C.-J. Pan, S. Bordère, D. Filimonov, C. Drathen, E. Suard, B.-J. Hwang, A. Wattiaux and C. Delmas, *J. Mater. Chem. A*, 2015, **3**, 10976–10989.
54 A. Maazaz, C. Delmas and P. Hagenmuller, *J. Incl. Phenom.*, 1983, **1**, 45–51.
55 B. Mortemard de Boisse, D. Carlier, M. Guignard, L. Bourgeois and C. Delmas, *Inorg. Chem.*, 2014, **53**, 11197–11205.
56 Z. Lu and J. R. Dahn, *J. Electrochem. Soc.*, 2001, **148**, A1225.
57 E. Talaie, V. Duffort, H. L. Smith, B. Fultz and L. F. Nazar, *Energy Env. Sci*, 2015, **8**, 2512–2523.
58 Y. H. Jung, A. S. Christiansen, R. E. Johnsen, P. Norby and D. K. Kim, *Adv. Funct. Mater.*, 2015, **25**, 3227–3237.
59 N. Sharma, E. Gonzalo, J. C. Pramudita, M. H. Han, H. E. A. Brand, J. N. Hart, W. K. Pang, Z. Guo and T. Rojo, *Adv. Funct. Mater.*, 2015, **25**, 4994–5005.
60 T. Ohzuku and A. Ueda, *J. Electrochem. Soc.*, 1994, **141**, 2972–2977.
61 I. Takahashi, K. Fukuda, T. Kawaguchi, H. Komatsu, M. Oishi, H. Murayama, M. Hatano, T. Terai, H. Arai, Y. Uchimoto and E. Matsubara, *J. Phys. Chem. C*, 2016, **120**, 27109–27116.
62 J. R. Croy, M. Balasubramanian, K. G. Gallagher and A. K. Burrell, *Acc. Chem. Res.*, 2015, **48**, 2813–2821.